Additives synergy for stable interface formation on rechargeable lithium metal anodes

Guorui Zheng [a,b], Yuxuan Xiang [a], Shijian Chen [a], Swapna Ganapathy [b], Tomas W. Verhallen [b], Ming Liu [b], Guiming Zhong [c], Jianping Zhu [a], Xiang Han [d], Weiwei Wang [a], Weimin Zhao [e], Marnix Wagemaker [b,**], Yong Yang [a,e,*]

[a] State Key Laboratory for Physical Chemistry of Solid Surfaces, Collaborative Innovation Center of Chemistry for Energy Materials, Department of Chemistry, College of Chemistry and Chemical Engineering, Xiamen University, Xiamen, 361005, PR China
[b] Department of Radiation Science and Technology, Faculty of Applied Sciences, Delft University of Technology, Mekelweg 15, Delft, 2629, JB, the Netherlands
[c] Xiamen Institute of Rare Earth Materials, Haixi Institutes, Chinese Academy of Sciences, Xiamen, 361021, PR China
[d] Semiconductor Photonics Research Center, Department of Physics, College of Physical Science and Technology, Xiamen University, Xiamen, 361005, PR China
[e] College of Energy, Xiamen University, Xiamen, 361005, PR China

ARTICLE INFO

ABSTRACT

The attention towards lithium (Li) metal anodes has been rekindled in recent years as it would boost the energy-density of Li batteries. However, notorious safety issues and cycling instability severely hinder their commercialization, especially when cycled in traditional carbonic ester electrolytes that exhibit a wide voltage window and are compatible with most of the cathode materials. Herein, lithium difluorophosphate (LiDFP) and vinylene carbonate (VC) are combined, and demonstrated to be synergistic in constructing *in situ* a mechanically stable and highly Li-ion conducting surface film on the Li metal anode. This results in uniform and compact Li deposition largely suppressing the formation of Li dendrites, dead lithium and irreversible Li-species as revealed by *operando* neutron depth profiling (NDP). This enables long-term cycling stability and enhancement of the Coulombic efficiency for rechargeable Li metal anodes. By combining solid state nuclear magnetic resonance (SSNMR) and spectroscopic studies, it is demonstrated that VC slows down the LiDFP reduction, yet promoting the breaking of the P–F bonds, which leads to a protective film. This film is rich in LiF–Li_3PO_4 inorganic compounds, distributed homogeneously, that is embedded in a matrix of P–O–C species and macromolecular organic compounds like lithium ethylene dicarbonate. This composition is responsible for the improved ionic conductivity and mechanical stability of the protective film during extended cycles. The detailed insight in the additives interaction provides new opportunities for the design of rational surface films necessary for realizing high-performance lithium metal batteries.

1. Introduction

In order to satisfy the ever-increasing demand for high-energy-density lithium (Li) batteries, development of advanced anode materials is essential. Among various anode materials, Li metal with an extremely high theoretical specific capacity (3860 mA h g^{-1}) and the lowest electrochemical potential (-3.04 V versus standard hydrogen electrode) is regarded as the ultimate anode, especially when paired with Li-free cathodes such as Li-oxygen and Li-sulfur [1,2]. However, until now the Li metal anode (LMA) is not primed for commercial application due to its poor cycle stability and safety hazards associated with Li dendrite formation, continuous side reactions and infinite volume changes [3,4]. To address these issues, it is critical to create a stable interface on the Li metal anode that results in a uniform distribution of the Li ion flux during repeated Li plating/stripping [5]. Significant progress has recently been achieved in surface and interface engineering of the Li metal anode, mainly through the construction of artificial protective films [6,7], liquid electrolyte modifications [8,9], solid-state electrolyte applications [10,

11], and Li host designs [12,13]. Of these strategies, controlling the compositions of the nonaqueous liquid electrolyte shows significant advantages being low cost, easy to implement and allowing better compatibility for practical batteries.

Due to the high intrinsic thermodynamic reactivity of Li metal with the organic electrolyte, the solid electrolyte interface (SEI) layer is expected to form instantaneously at the liquid organic electrolyte/Li metal anode interface [14]. As reported, the accumulation of this highly resistive layer in the liquid electrolyte may be the main reason for the observed early cell's death, even before dendrites short circuit the battery [4,15]. To avoid this scenario, a good quality SEI layer is required. This SEI should have the ability to manipulate the migration path of Li ions and realize uniform Li deposition. It should also possess good mechanical robustness and elasticity to resist infinite volume change and suppress dendrite formation [16,17]. The composition of the hierarchical SEI formed in traditional alkyl carbonic ester electrolytes is comprised mostly of relatively small Li salts. These cannot tolerate the morphological change of the Li surface during Li deposition/dissolution, and this leads to low cycling efficiency and dendrite formation [14]. Although carbonic ester electrolytes are more reactive with Li metal, compared to ether-based electrolytes, they are relatively stable against oxidation, which leads to their compatibility with a charge cutoff voltage exceeding 4.0 V [18]. In this context, there is considerable interest in optimizing film-forming additives in carbonic ester electrolytes to form *in situ* a stable SEI that prevents continuous electrolyte decomposition.

Fluorine (F) containing species in the electrolytes have been extensively studied for their ability to form relatively stable interfaces on rechargeable lithium metal anodes [19]. Examples of this includes the application of lithium bis(trifluoromethanesulfonyl)imide (LiTFSI) [20–22], lithium bis(fluorosulfonyl)imide (LiFSI) [23–27], lithium hexafluorophosphate (LiPF$_6$) [28,29], and fluoroethylene carbonate (FEC) respectively [30–32]. LiPF$_6$ as an additive to carbonate solvents has been confirmed to enhance the charging capability and cycling stability of Li metal batteries due to the generation of a robust and conductive SEI layer comprising of polycarbonates [28]. These are derived from the ring-opening polymerization of the ethylene carbonate (EC) solvent induced by the catalytic reaction of PF$_5$ and POF$_3$. Coincidentally, lithium difluorophosphate (LiDFP), an inorganic additive having a O–P–F structure derived from the hydrolysis of LiPF$_6$, has been used for improving the performance of Li ion batteries by modifying the interface between the electrode and electrolyte [33,34]. Recently, the efficacy on rechargeable Li metal anodes has been reported when used in conjunction with carbonic ester electrolytes [35]. However, the improvement of electrochemical properties are limited and the modification mechanism has not been revealed. A very frequently applied cyclic carbonate organic additive is vinylene carbonate (VC) which has a similar structure to EC, and has been reported to suppress side reactions by forming a surface film consisting of polymeric species [36,37]. Based on the complementary advantages, combining the LiDFP and VC additives to a carbonic ester electrolyte can therefore be suggested to *in situ* form a flexible and robust hybrid SEI layer.

Here, we report the synergetic effect of LiDFP and VC in stabilizing the lithium metal surface in a carbonic ester electrolyte to enable better performance of rechargeable lithium metal anodes. *Operando* neutron depth profiling (NDP), a non-invasive and non-destructive tool selectively sensitive to ^{6}Li via its capture reaction with thermal neutrons, is used to monitor the SEI formation and the evolution of the lithium metal layer during plating and stripping cycles [38–41]. Complementary multinuclear magic angle spinning (MAS) solid-state nuclear magnetic resonance (SSNMR) measurements and X-ray photoelectron spectroscopy (XPS) provide insight in the SEI composition formation. Combined with electrochemical measurements, structural characterization and componential detection, this demonstrates the formation of a highly uniform, stable and ionic conductive SEI layer. This in turn leads to the reversible formation of a dense and uniform Li morphology on plating and dramatic improvement in the cycling lifetime and Coulombic

efficiency (CE) of the Li metal anode in the carbonic ester electrolyte.

2. Experimental section

2.1. Preparation of electrolytes

All the materials are in battery-grade purity. The commercially available lithium difluorophosphate (LiPO$_2$F$_2$, LiDFP) was ordered from Zhejiang Sinochem Lantian Co. Ltd (China). Both of the vinylene carbonate (VC) and the mixed electrolytic solvent of ethylene carbonate (EC)-ethyl methyl carbonate (EMC) in a 3:7 ratio by weight were purchased from Zhuhai Smooth Way New Materials Co. Ltd (China). The lithium perchlorate (LiClO$_4$) (Morita Chemical Industries (Zhangjiagang) Co. Ltd., China) was used as the electrolytic salt to avoid the influence of its decompositions. The base electrolyte (EC/EMC) of 1.0 M LiClO$_4$ in a mixed electrolytic solvent was prepared in an argon-filled glove box (both of the O$_2$ and H$_2$O were restricted below 0.5 ppm). 2 wt% LiDFP additive and/or 2 wt% VC additive were dissolved into the EC/EMC to get a set of electrolytes.

2.2. Electrochemical measurements

For evaluating the interfacial modification on rechargeable lithium (Li) metal anodes (LMAs) with dual-additive electrolyte, different electrochemical measurements were carried out using CR2025 coin-type half-cells of Cu/Li and symmetrical Li/Li that were assembled in an argon-filled glove box with Li metals (Φ 14 mm, 350 μm thick, from China Energy Lithium Co. Ltd.) as the counter electrodes and Celgard 2300 as physical separators. The assembled Cu/Li cells were tested galvanostatically by setting corresponding discharge capacity of 1 mA h cm^{-2} in Li plating process and charging voltage to 1 V for Li stripping process at a constant current density of 0.5 mA cm^{-2}. The symmetrical Li/Li cells were operated at a fixed current density of 0.5 mA cm^{-2} with a total capacity of 1 mA h cm^{-2}. Both kinds of coin cells were measured on a Land CT2001A system at the temperature of 30 °C. Cyclic voltammetry (CV) experiments were conducted at a scan rate of 0.1 mV s^{-1} and a potential range of 0 V–2.5 V (vs. Li$^+$/Li) on a four-channel multifunctional electrochemical work station (PARSTAT MC). Electrochemical impedance spectroscopy (EIS) experiments were measured over the frequency ranges from 1 MHz to 10 mHz with an alternative current amplitude of 10 mV on a electrochemical work station (Solartron 1260).

2.3. NDP detection and data handling

A pouch cell was fabricated with ~10 μm thick Cu foil as the working electrode and the window towards the NDP detector. The separator used was a 25 μm PE (Celgard) sheet against window and a 300 μm glass fiber (Whatman). In total, 180 μL electrolyte prepared as abovementioned was added to the separator. Approximately 500 μm rolled Li-metal foil, 95 wt % ^{6}Li and 5 wt% ^{7}Li (density 0.47 g cm^{-3}, from Sigma Aldrich), serves as both the counter electrode and reference electrode. Electrolyte enrichment is achieved by exposure to an abundance of ^{6}Li metal (95 wt% pure), before used in the *operando* NDP cells. Measurements were performed in a helium filled chamber. Then the assembled pouch cell was inserted into a homemade set-up, which was updated by fresh helium for about 7 min to avoid reducing pressure leading to the failure of *operando* NDP cell. The set-up consists of an aluminum vacuum chamber where a Canberra PIPS detector is placed at 4 cm from the pouch cells in order to detect particles that are leaving the pouch cell perpendicular to the battery electrodes and is also used to measure the energy of the emitted particles. Galvanostatic cycling was performed by deposition of Li onto the Cu working electrode up to a capacity of 1 mA h cm^{-2}, followed by Li stripping up to 1 V at a constant current density of 0.5 mA cm^{-2}. NDP was performed on the dedicated beam line at the Reactor Institute Delft. The stable isotope ^{6}Li can undergo a neutron capture reaction. This reaction between a neutron and the atoms' core produces two new particles, He^{2+}

(E_k = 2044 keV) and $^3H^+$ (E_k = 2727 keV), emitted in all directions. As these particles travel through the sample, energy is lost to interactions with surrounding electrons. Due to the higher mass and valence state as well as their lower initial energy the helium ions experience a larger stopping power, which prevents them from reaching the detector in the demonstrated experiments [42]. By placing the detector at 4 cm distance from the sample only tritons (^3H) with perpendicular trajectories reach the detector. The energy loss of the ^3H particles is measured with the charged particle implanted Si detector having a resolution of 3.3 keV. The energy spectrum is then collected by a Multi-Channel Analyzer. Decided by the stopping power of the materials remaining in the transporting path of $^3H^+$, the depth where the $^3H^+$ comes out is calculated. Changes in the stopping power due to the formation of the metal layer are expected to be compensated by the formation of the SEI layer. Furthermore energy straggling induced by the copper foil and helium environment invalidates a sub-micron analysis of the plated layer [43,44]. The resolution for these systems is approximately 1 μm.

2.4. Materials characterization

The Cu foil-based LMAs for characterizations at different cyclic states were retrieved from Cu/Li cells, cleaned with pure EMC for three times to remove the residual salts, finally dried overnight under vacuum at room temperature and transferred by a relevant sealed container filled with argon to avoid side reactions or electrodes contamination with ambient oxygen and moisture. For structural observation of lithium metal layers during cycling, field emission scanning electron microscopy (SEM, HITACHI S-4800) coupled with an energy dispersive X-ray spectrometer (EDS) was supplied to characterize the morphologies, structures and surface elemental distribution of Li metal layers deposited on Cu substrates after different cycles when cycled in the electrolytes with different additives. Furthermore, atomic force microscopy (AFM, Agilent 5500) were used in an argon-filled glove box to explore the structure and mechanical response of the surface films formed at different electrolytes. For chemical compositions detection of SEI layers formed on Cu foil-LMAs, different spectrum analysis technologies were combined complementarily. Fourier transmittance infrared (FTIR) spectroscope was used for recording the FTIR spectra of the samples in the range of 400–4000 cm^{-1} on a Nicolet 6700 spectrometer by diffuse reflection mode. A homemade cell with a self-supporting wafer loaded in the middle and CaF$_2$ windows was constructed to avoid ambient contamination when transferring and testing. X-ray photoelectron spectroscopy (XPS) spectra were acquired with PHI-5000 Versa Probe II spectrometer (ULVAC-PHI, Inc., Japan) with monochromatic Al Kα 1486.6 eV radiation, operating at 25 W and in a vacuum of <10^{-8} Torr. The universal contamination of the C–H bond at 284.8 eV was used as a reference for the final adjustment of energy scale in the spectra and the peaks were fitted using the XPSPEAK software. *Ex situ* multinuclear solid-state nuclear magnetic resonance (SSNMR) experiments were performed on a Bruker Ascend 11.7 T (500 MHz) magnet with a NEO console at room temperature. ^6Li chemical shifts were externally reference to 1 M LiCl aqueous solution (^6Li 0 ppm), ^{31}P to 1 M Li$_3$PO$_4$ aqueous solution (^{31}P 0 ppm) and ^{19}F to LiF powder (^{19}F −204 ppm). The ^6Li spectra were acquired with a ^6Li Larmor frequency of 73.60 MHz using Bruker 4 mm double-resonance magic angle spinning (MAS) NMR probe with a spinning frequency up to 10 kHz using direct polarization with a pulse length of 4.7 μs and a recycle delay of 120 s. The ^{31}P spectra were acquired with a ^{31}P Larmor frequency of 202.47 MHz using Bruker 4 mm probe at spinning rate of 10 kHz through a hahnecho sequence with a pulse length of 4.5 μs and a recycle delay of 40 s. The ^{19}F spectra were acquired with a ^{19}F Larmor frequency of 470.56 MHz using Bruker 1.9 mm probe at different spinning rates of 20 kHz, 25 kHz and 30 kHz through a hahnecho sequence with a pulse length of 2 μs and a recycle delay of 10 s.

3. Results and discussion

3.1. Lithium metal plating/stripping cycling performance

To evaluate the effect of additives on electrochemical cycling performance, Cu/Li coin cells were assembled and galvanostatic measurements were conducted (see **Experimental Section** for the details). The CE is defined as the capacity of lithium stripped divided by the capacity of lithium plated on the Cu foil based on the integrated current, which determines the lithium loss during cycling [45]. As shown in Fig. S1, the coin cells with only the LiDFP additive exhibit a limited enhancement in CE and cycling lifetime. The optimal amount of LiDFP additive is determined to be 2 wt%. Despite the limited improvement, it is critical to understand the interface modification mechanism induced by the LiDFP additive. A high concentration of lithium salt was reported to enhance the lithium ion (Li$^+$) transfer number, which leads to a more uniform deposition of Li metal [22,26,29]. To test this hypothesis, rather than using the LiDFP additive, higher concentrations of LiClO$_4$ were also tested as shown in Fig. S1. From the deteriorating cycle performance in Cu/Li coin cells with increasing Li$^+$ concentrations, it can be concluded that the improvement observed for the LiDFP-added electrolyte has a different origin.

Aiming at improved long-term cycle performance, 2 wt% VC is added to the base carbonic ester electrolyte (denoted as EC/EMC) in addition to 2 wt% LiDFP. As shown in Fig. 1a, the individual additives improve the first cycle CE from 54.7% to 87.5% and 86.5% for LiDFP (denoted as LiDFP-EC/EMC) and VC (denoted as VC-EC/EMC) respectively. Nevertheless, a sudden drop in the CE is observed for both individual additives upon subsequent cycling. In contrast, the Cu/Li coin cells using the electrolyte with both LiDFP and VC additives (denoted as LiDFP-VC-EC/EMC) exhibits dramatic improvements in CE (initial CE reaches to 90.4%) and cycling lifetime. After 80 cycles, the cells maintains a CE of around 95% demonstrating the best cycling stability, indicating a synergistic effect of the two additives.

The dramatic improvement in cycling stability is also evident from the voltage profiles. As shown in Fig. S2, the voltage hysteresis of Cu/Li coin cells with EC/EMC electrolyte increases gradually due to the formation of an unstable interface layer, continuous electrolyte depletion and accumulation of inactive species, which raise the resistance. For the LiDFP-EC/EMC electrolyte, the voltage hysteresis is smaller and the CE during the first cycles is clearly enhanced compared to cells with EC/EMC, indicating that a lower resistance and formation of a more stable interface, which however appears to degrade already after 20 cycles. For the VC-EC/EMC electrolyte, the largest voltage hysteresis is found indicating the formation of a highly resistive interface between electrolyte and Li-metal anode. However, the cycling stability during the first cycles is also better than the cells without additive. For the Cu/Li coin cells with LiDFP-VC-EC/EMC electrolyte, the voltage curves almost overlap even after 80 cycles, demonstrating its high interfacial stability and low resistance.

Symmetrical Li/Li cells were assembled to evaluate the efficacy of the combined LiDFP and VC additive that appear synergistic in stabilizing the Li metal anode/electrolyte interface. Typical long-term galvanostatic cycling results obtained by monitoring the changes in voltage polarization and interfacial resistance are displayed in Fig. 1b. After being cycled for *ca.* 300 h, the cells with EC/EMC electrolyte show significant fluctuation in the voltage profile. Such huge hysteresis implies the formation of an unstable and highly resistive interfacial layer caused by continuous side reactions and an increasing amount of inactive Li. For the cells with LiDFP-EC/EMC electrolyte, a smaller voltage hysteresis and more stable cycling is observed until *ca.* 480 h. Despite having the largest voltage polarization, the cells with VC-EC/EMC electrolyte also show an enhanced lifetime of *ca.* 480 h. In contrast, the cells cycled in LiDFP-VC-EC/EMC electrolyte show low voltage hysteresis for an extensively improved lifetime of exceeding 800 h. A potential explanation is the stabilization of the Li metal anode/electrolyte interface and a more

G. Zheng et al.
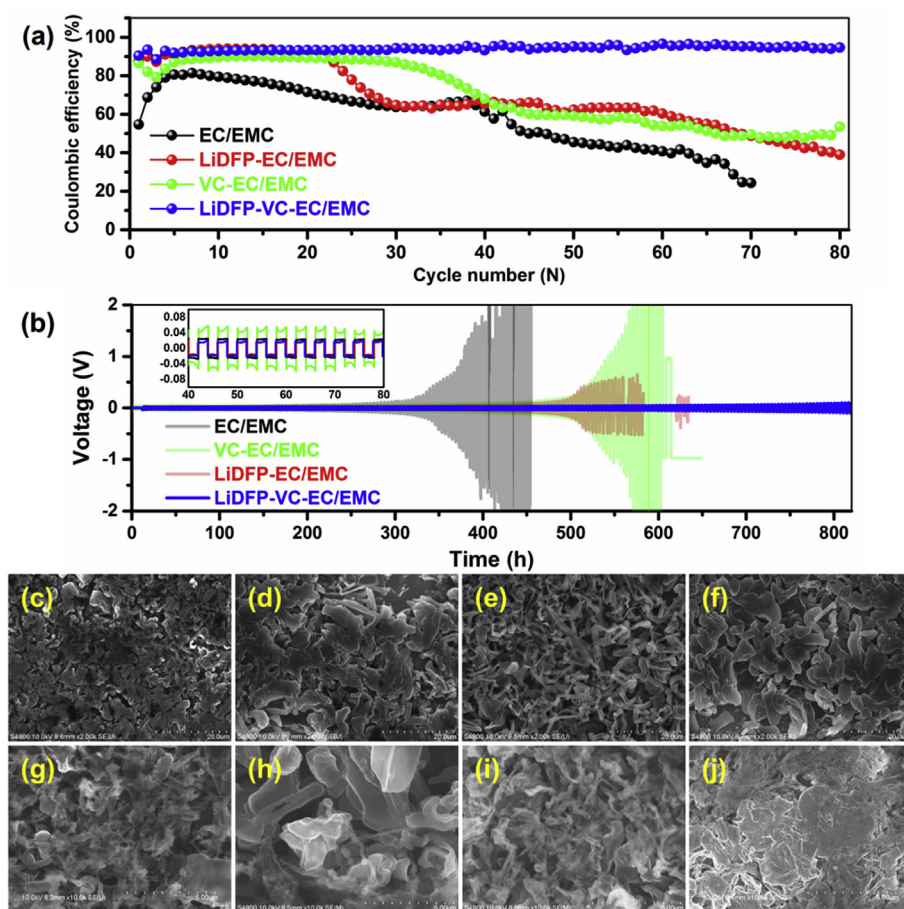
Fig. 1. Electrochemical stability and microstructural evolution of lithium metal anodes during cycling. a) Cycling efficiency of Cu/Li coin cells with the EC/EMC base carbonic ester electrolytes with different additives during cycling to a constant discharge capacity of 1 mA h cm^{-2} (Li metal plating) and charging to a maximum charge potential of 1 V vs Li/Li$^+$ (Li metal stripping) at a constant current density of 0.5 mA cm^{-2}. b) Voltage stability of symmetrical Li/Li coin cells using EC/EMC electrolytes with and without different additives at a fixed current density of 0.5 mA cm^{-2} to a total capacity of 1 mA h cm^{-2}. c-j) SEM images of morphologies of lithium metal layers on the Cu substrates after the first (c–f) and 20th (g–j) plating cycle in different electrolytes. (c, g) EC/EMC, (d, h) LiDFP-EC/EMC, (e, i) VC-EC/EMC, and (f, j) LiDFP-VC-EC/EMC.

homogeneous lithium metal plating/stripping process. This can be qualitatively confirmed by comparing the scanning electron microscopy (SEM) images of the Li-metal deposits after the 1st and 20th plating cycle, shown in Fig. 1c–j. Depending on the electrolyte used, there are noticeable differences in the morphology of the Li metal deposits. After the first Li plating (Fig. 1c–f), use of EC/EMC leads to the formation of out-of-shape, small sized loose structures (Fig. 1c), from which short Li metal fibres are sporadically discernible. The Li deposited in LiDFP-EC/EMC (Fig. 1d) is also non-uniform but has larger sized particles, which decrease the specific surface area towards the electrolyte reducing the amount of side reactions, responsible to the high initial CE and more stable cycling performance observed compared to the Cu/Li cells with EC/EMC. In sharp contrast, the core of the lithium metal layer in VC-EC/EMC (Fig. 1e) is constructed of interlaced lithium fibers several micron in length and with a diameter of about 500 nm. Such a structure may increase the probability of dead Li remaining on stripping and a lower lifetime during long-term cycling despite the high initial CE. For the LiDFP-VC-EC/EMC (Fig. 1f), the deposited Li exhibits more smooth and uniform deposition existing of well-defined particles with an average size of about 5 μm. After the 20th Li plating (Fig. 1g–j), the Li metal layer on Cu foil cycled in LiDFP-VC-EC/EMC maintains the smooth, dense and uniform morphology and no Li dendrite formation is observed, which can also be further confirmed by comparing the cross-section SEM images shown in Fig. S3. To gain more insight in the impact of the different additives on the evolution of these deposits, the Li-density is investigated with *operando* NDP.

3.2. Operando NDP measurement for evolution of Li metal anode

The Li-metal and SEI morphology during Li plating and stripping in

Cu/Li pouch cells with different electrolytes is monitored in real time with *operando* NDP measurements. This enables a direct quantitative insight in the Li-metal density distribution and reversibility, providing understanding of the influence of the different additives on the evolution of the Li metal anodes. Fig. 2 shows the *operando* NDP results of the first 5 cycles at 0.5 mA cm^{-2} during capacity limited cycling up to a plating capacity of 1 mA h cm^{-2} during which the lithium concentration profiles were obtained every 90 s. The measured intensity and energy loss of the ^{3}H$^+$ that reaches the detector is converted into the Li-density through the stopping power as described in the **Experimental Section**, where the practical depth resolution is approximately 1 μm, dominated by the straggling of the ^{3}H$^+$ particles in the Cu current collector. For convenience, the surface of the Cu window facing the electrolyte was set as the zero depth as reference for the Li-density depth profiles. Fig. 2a–d shows the *operando* NDP results for the cell using base electrolyte without additive. From the 2D Li density map in Fig. 2b, showing the Li density as a function of depth during the first 5 cycles, it is observed that a relatively large density of inactive Li species remains after the first full cycle, consistent with the low initial CE. During repeated cycling the Li density after plating and after stripping propagates progressively deeper into the liquid electrolyte, which reflects the continuous accumulation of inactive lithium species most likely including Li containing SEI species as well as dead Li metal. In combination with the porous Li-metal deposits, this can be held responsible for the poor cyclic stability and low CE shown in Fig. 2a. Fig. 2b also indicates that the Li plating and stripping process is asymmetric, which can be more clearly visualized through the plating and stripping activity, the depth resolved change in Li concentration as a function of time, as shown in Fig. 2c–d. During the Li plating, the position where the Li deposition takes place progressively moves away from the Cu substrate into the electrolyte, which is in accordance with root growth
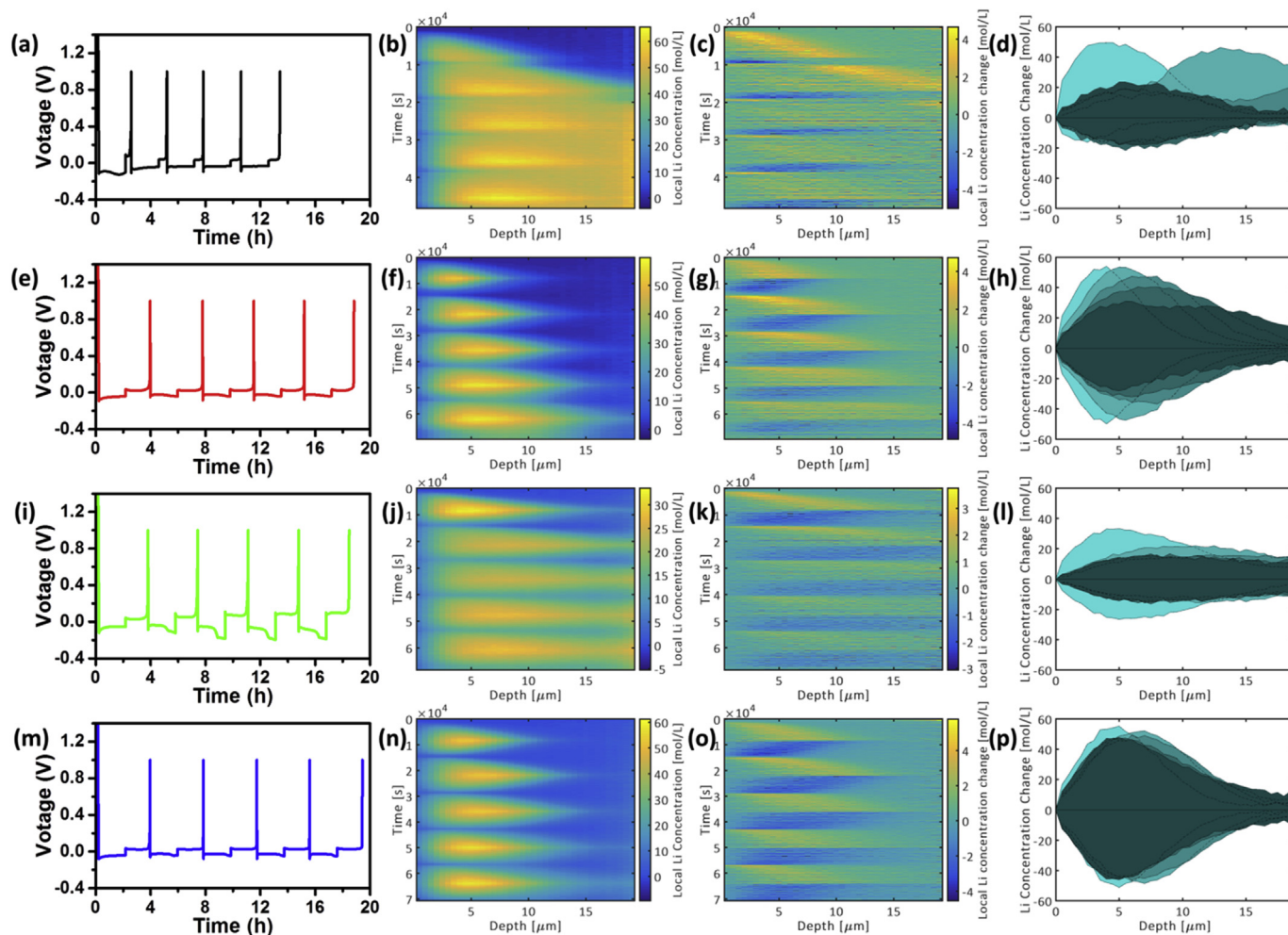
Fig. 2. *Operando* NDP measurements of Cu/Li pouch cells during the initial five cycles at 0.5 mA cm⁻² for understanding the impact of different additives on the Li plating and stripping. Electrochemical performance (a, e, i, m), depth resolved Li-density as a function of cycling resulting from *operando* NDP (b, f, j, n), Li-plating and stripping activity derived from the time derivative of the Li-density (c, g, k, o) and the change in Li concentration at the end of each discharge and charge of the cells (d, h, l, p) using the base carbonic ester electrolyte (EC/EMC) with and without different additives. (a–d) EC/EMC, (e–h) LiDFP-EC/EMC, (i–l) VC-EC/EMC, and (m–p) LiDFP-VC-EC/EMC. The density of pure Li-metal is around 67.7 mol L⁻¹.

of mossy Li pushing Li metal layer into the electrolyte. This mossy Li-metal growth will continuously expose fresh Li-metal towards the electrolyte inducing continuous SEI formation and hence electrolyte decomposition. In contrast to the plating, the stripping activity takes place rather homogeneously in depth over the porous Li-metal deposit, especially the part near to the surface of Cu window, which promotes the formation of islands of so called "dead Li-metal" electronically isolated from the current collector. As clearly observed in Fig. 2c during the second plating cycle, the plating activity starts at the depth position where the first plating ended, and the third starts where the second ended, as a consequence moving outside the maximum depth probed by the NDP. This implies that for the EC/EMC electrolyte the porous Li-deposit quickly grows into the electrolyte over repeated cycling, which can be considered the signature for early cell death due to a short circuit and the buildup of a highly Li-ion resistive deposit. For the LiDFP-EC/EMC electrolyte, the *operando* NDP results, shown in Fig. 2e–h, demonstrate that the addition of LiDFP induces the formation of more dense and uniform Li deposits and it reduces the amount of inactive Li to some extent. During the first cycle, the stripping activity is more localized starting at the top of the Li deposits, resulting in a more symmetric plating-stripping activity, which suppresses the formation of dead Li. Nevertheless, upon repeated cycling, the Li metal deposit grows thicker

and the stripping becomes more homogeneous, leaving an increasing amount of inactive Li behind. As shown in Fig. 2i–l, the addition of VC has a very different impact, as it results in very thick porous deposit already during the first cycle, which quickly extends beyond the maximum depth that can be detected by NDP. Still the plating and stripping appears more reversible as compared to the base electrolyte, leading to the higher Li efficiency in the early cycles. The more stable cycling implies a mechanically more stable SEI, however the high over-potential indicates poor ionic conductivity as compared to the SEI formed upon the LiDFP additive. The complementary impact of the additives on the Li deposit and SEI formation rationalizes to combine these additives, the results of which are shown in Fig. 2m–p. In this case, the plating remains dense over cycling, the plating and stripping activity remains symmetric at least during the first five cycles, and the accumulation of inactive Li species is obviously suppressed leading to highest Li efficiency compared to other electrolyte systems discussed above. The improved reversibility of the Li deposit indicates that the advantages of the individual additives are combined to result in an SEI that is both highly conductive and mechanically stable. To gain insight in the origin of these improvements the (electro)chemical nature of the deposits is investigated systematically with electrochemical measurements, energy dispersive X-ray spectroscopy (EDS), Fourier transform infrared

spectroscopy (FTIR), XPS and MAS SSNMR.

3.3. Characterization of the SEI layer

To understand the impact of two additives on the reductive decomposition of the electrolyte and SEI formation, the cyclic voltammetry (CV) curves are compared in Fig. 3a. An irreversible reduction peak appears around 1.0 V for the additive free EC/EMC electrolyte, indicating the decomposition of the EC and EMC solvents. This peak decreases on adding LiDFP and/or VC, demonstrating that these additives suppress the EC/EMC reduction. For LiDFP-EC/EMC, a new broad peak centered at about 1.4 V appears, which can be assigned to the reduction of LiDFP. The small decomposition peak of VC centered at about 1.7 V can be seen according to the curves from VC-EC/EMC. On adding LiDFP and VC simultaneously, the reduction peaks of the electrolytic solvents and additives further decrease, reflecting the improved SEI properties due to the synergistic effect of the two additives. To further study the electrochemical properties of the SEI layer, electrochemical impedance spectra (EIS) of Cu/Li coin cells were recorded after the 20th stripping, as shown in Fig. 3b. One asymmetrical semicircle is observed in the high to mid-frequency range, corresponding to the total resistance due to the SEI film, interphase contact and charge transfer. Thus, the diversity of the impedance curves derives from the kinetic characteristics of Li^+ deposition on the substrate and the nature of the SEI films. As expected, the addition of LiDFP decreases the resistance of the SEI which promotes homogeneous Li metal plating, whereas the VC additive has the opposite consequence, also compromising resistance when the two additives are combined. To evaluate the mechanical properties of the SEI films, nanoscale indentation was carried out with an atomic force microscope (AFM) [46]. Fig. S4 shows the AFM-force curves of the SEI films on Cu foil-based LMAs after the 20th plating. The slope of external load versus depth profile can be related to the surface contact stiffness of the SEI layer [47], which is summarized in Table S1. The contact stiffness of the SEI layer on Cu foil-based LMA cycled with the dual-additive electrolyte is lower than that of the SEI without additive and with the LiDFP additive alone and higher than that of SEI with only the VC additive. This indicates that the SEI layer formed in LiDFP-VC-EC/EMC is more flexible than that formed without VC, preventing the exposure of fresh electrolyte, and more

conductive for Li^+ than that formed without LiDFP making it less prone to dendrite formations.

Both EDS and FTIR measurements were conducted to comprehensively analyze the components of the SEI formed on the Cu foil-based LMAs cycled in electrolytes with different additives. The elemental distribution after the 1st cycle plating determined by EDS shown in Fig. 3c demonstrates that the co-addition of LiDFP and VC to the electrolyte suppresses the consumption of LiDFP. After the 20th plating, there is a higher amount of carbon, P and F homogeneously distributed over the surface of the Cu foil-based LMAs that were cycled in the dual-additive electrolyte, as shown in Fig. S5. In addition, the content ratio of C to O increases, suggesting the formation of more organic species as compared to the addition of only LiDFP, leading to a more flexible SEI layer. The FTIR results for the dual additive after the 20th stripping, shown in Fig. 3d, demonstrates that the SEI is rich in P–O–C species and lithium ethylene dicarbonate and that there is relatively a small amount of Li_2CO_3 [32]. For the LiDFP-added electrolyte, the components of the surface film mainly contain Li_2CO_3 and relatively small amounts of P–O–C species and lithium ethylene dicarbonate. For the VC-added electrolyte, the dominating components of the surface film are Li_2CO_3, lithium methyl carbonate and lithium ethylene dicarbonate. For the base electrolyte, there are more inorganic species present like Li_2CO_3 and low molecular weight organic species like lithium methyl carbonate. These results suggest that P–O–C species and macromolecular organic compounds like lithium ethylene dicarbonate, combined with smaller amounts of Li_2CO_3, play an important role in improving the mechanical stability and ionic conductivity of the SEI layer during prolonged cycling. However, complementary characterization needs to be carried out to further confirm the composition of the surface films and to understand the formation mechanism of the SEI layer, especially in the presence of both the LiDFP and VC additives.

XPS analysis was carried out to characterize the chemical composition of the respective SEIs formed on the Cu foil-based LMAs with different electrolytes after the 1st lithium plating and the 20th lithium stripping. The C 1s and O 1s spectra from the electrolytes with additives, shown in Fig. S6, demonstrate that after 20 cycles there are more organic species as compared to the XPS spectra after the 1st deposition process, consistent with the FTIR results. The C 1s spectra for the base electrolyte
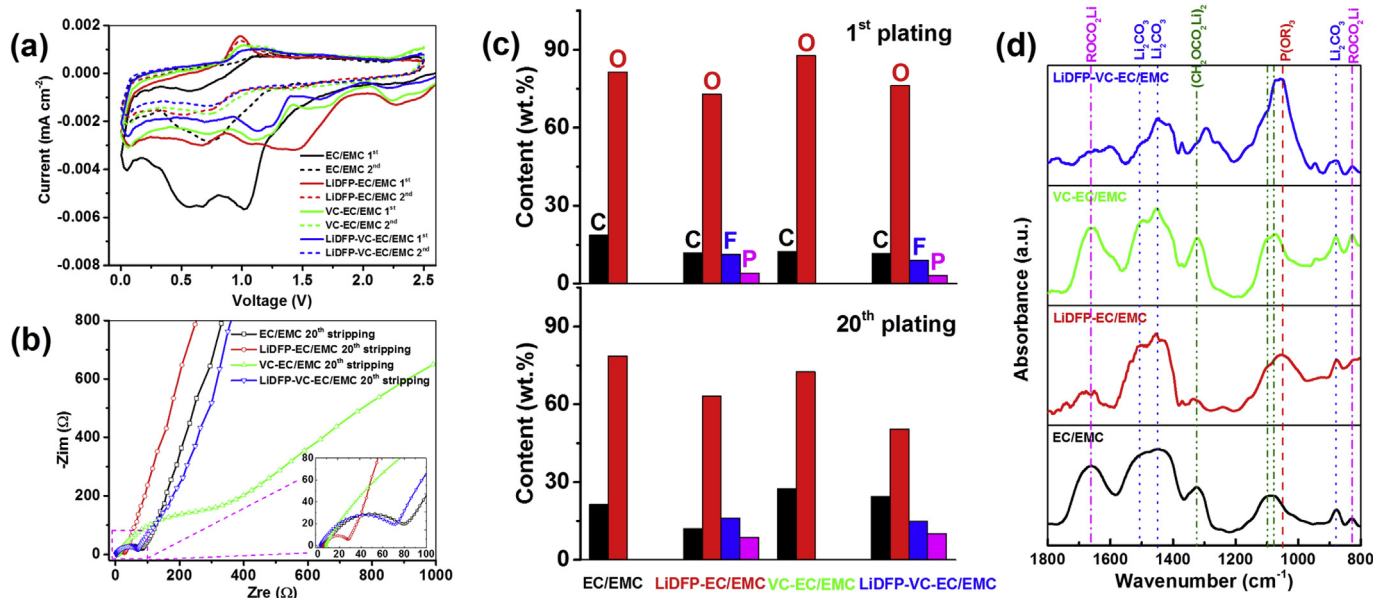
Fig. 3. Electrochemical behavior and characterization of SEI components formed in different electrolytes. a) CV curves of Cu/Li coin cells with the carbonic ester electrolyte (EC/EMC) containing different additives at a scan rate of 0.1 mV s^{-1} and a potential range of 0 V–2.5 V (vs. Li$^+$/Li) for the first 2 cycles. b) EIS of Cu/Li coin cells with different electrolytes after the 20th cycle Li stripping. c) Comparison of the percentages of elements identified in cycled Cu foil-based LMAs after the 1st and 20th cycle Li plating via EDS spectra. d) FTIR spectra of surface films left on the Cu substrates retrieved from the cells after the 20th cycle Li stripping.

demonstrates the abundance of inorganic compounds like Li_2CO_3 in the SEI layer after 20 cycles, leading to a low ionic conductivity, brittleness and lack of adhesion with the underlying metal surface. This can be expected to lead to easy rupture of the SEI leading to the exposure of fresh electrolyte. In contrast, the presence of LiDFP results in only a small amount of Li_2CO_3 in the SEI after 20 cycles, which can be expected to be beneficial for the Li-ion conductivity through the SEI layer. Fig. 4a–h exhibits a comparison of the Li 1s spectra of the SEI layer formed in different electrolytes, which demonstrates that the main Li-containing species in all samples are Li_2CO_3 and $ROCO_2Li$ whereas LiF and Li_3PO_4 are only found in the LiDFP-containing electrolytes. Interestingly, after the 20th Li stripping, the content of Li_2CO_3 decreases in the LiDFP-added electrolytes. This indicates that the decomposition components in the electrolyte are influenced by the LiDFP additive by the extended cycling, in this case resulting in an SEI that is more flexible and better conducting. Fig. 4i–p shows a comparison of the P 2p and F 1s spectra of the SEI layer for the LiDFP additive and for the combined LiDFP and VC additive after the 1st plating and 20th stripping. For the dual additive almost all the P-containing species in the SEI layer represent P–O species, the amount of which strongly increases after the 20th stripping, indicating that the LiDFP additive is reduced to become part of the components of the SEI layer. However, when only the LiDFP additive is present, there are more O–P–F species present in the SEI, especially after the 20th stripping. This demonstrates that the P–F bond in the LiDFP additive is more easily broken in the presence of VC, where it should be expected that each

LiDFP molecule releases two F atoms under the co-addition of VC, which is supported by comparison of the F 1s spectra. The main F-containing species in the SEI layer in the dual-additive electrolyte is LiF, which contributes to the improved mechanical strength and stability. In addition, the amount of LiF in LiDFP-VC-EC/EMC is less than that in LiDFP-EC/EMC, indicating that VC is beneficial for limiting the excessive consumption of LiDFP and supporting mechanical stability without the existence of large amount of LiF. As is expected, upon cycling the electrolyte in the presence of only the LiDFP additive the amount of O–P–F species increases, suggesting that it is increasingly difficult to break the P–F bonds during continuous cycling. Therefore, since the SEI layer is less flexible and stable without addition of VC, the more LiF is needed to repair the SEI layer to strengthen its framework. However, this cannot be realized with only adding LiDFP additive.

MAS SSNMR was used to further analyze the SEI components after the 20th lithium stripping, which has the advantage to be especially sensitive to the P and F chemical environments and detect the complete SEI layer, rather than the top layer, thereby providing complementary information concerning the SEI formation mechanism and its properties. As shown in Fig. 5a, all the samples show a [6]Li resonance centered around 264 ppm and an asymmetrical peak centered at around 0 ppm [48]. The former is assigned to dead metallic Li, indicating sectional capacity loss during cycling, most prominently present for the electrolytes without the LiDFP additive. The [6]Li resonance around 0 ppm is assigned to lithiated species in the SEI, the deconvolution of which is shown in Fig. 5b. For
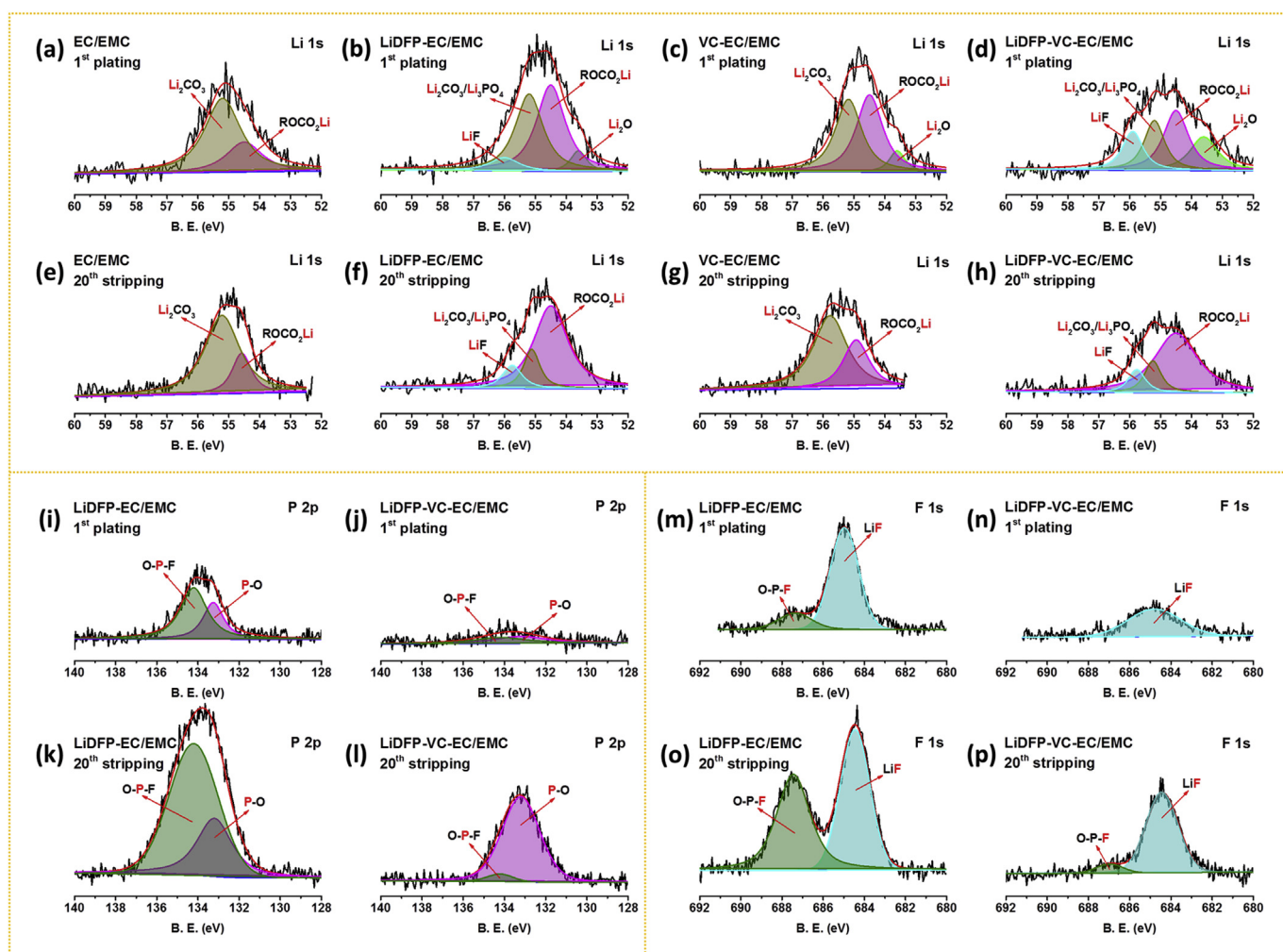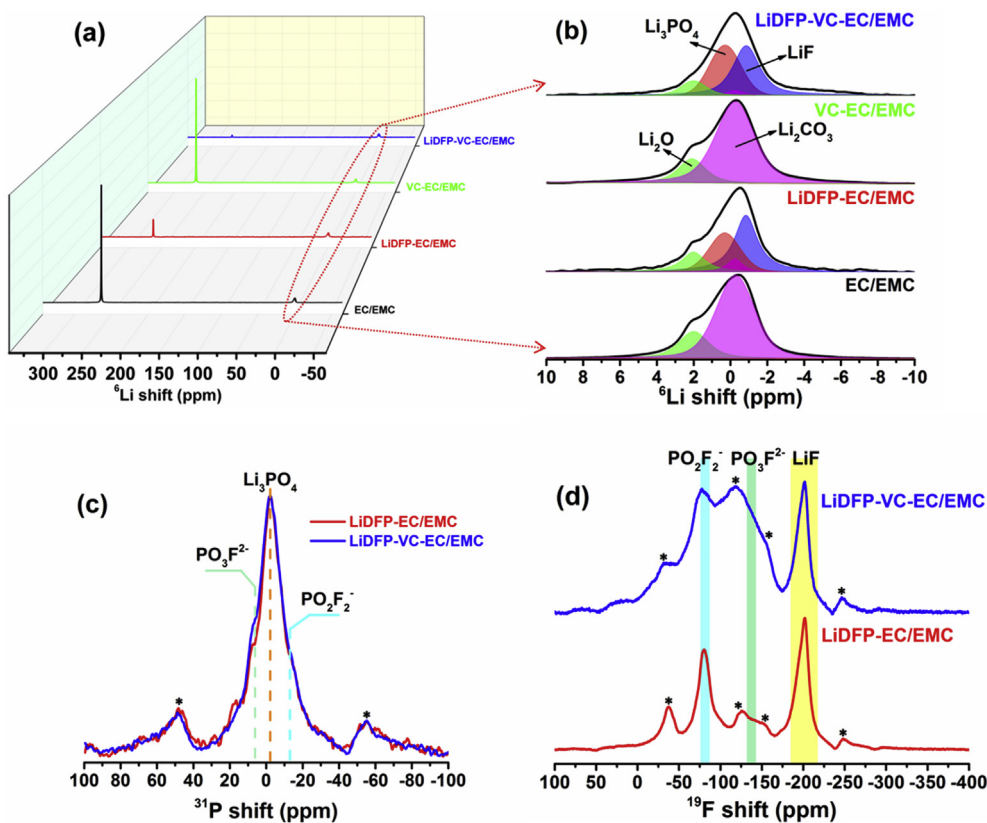

Fig. 4. Chemical composition of the surface films on the cycled Li metal anodes. Li 1s (a–h), P 2p (i–l) and F 1s (m–p) XPS spectra of the SEI layers formed on the Cu foil-based LMAs after the 1st Li plating (a-d, i-j and m-n) and 20th Li stripping (e-h, k-l and o-p) with different electrolytes. (a, e) EC/EMC, (b, f, i, k, m, o) LiDFP-EC/EMC, (c, g) VC-EC/EMC, and (d, h, j, l, n, p) LiDFP-VC-EC/EMC.

Fig. 5. Chemical components of the surface films formed on the cycled Li metal anodes. MAS SSNMR spectroscopic analysis of the residues formed on the Cu substrates recovered from the cells with different electrolytes after the 20th cycle Li stripping. (a, b) ^{6}Li MAS SSNMR spectra, (c) ^{31}P MAS SSNMR spectra, and (d) ^{19}F MAS SSNMR spectra. The spinning sidebands are marked with asterisks (*).

LiDFP-EC/EMC and LiDFP-VC-EC/EMC, both surface films mainly comprise of LiF and Li$_3$PO$_4$, where the latter will be beneficial for the ionic conductivity as compared to conventional SEI species such as Li$_2$CO$_3$ and Li$_2$O *etc.* In contrast, for EC/EMC and VC-EC/EMC, the dominant SEI components are Li$_2$CO$_3$ and Li$_2$O, which reflects a brittle and poorly Li-ion conducting surface film. The P-containing and F-containing species derive from the reductive decomposition of the LiDFP additive [49], which is highly influenced by the co-addition of VC, as observed from Fig. 5c–d. The ^{31}P spectrum shows a main resonance centered at around −2.1 ppm representing Li$_3$PO$_4$ with two shoulders at 7.1 ppm and −13.3 ppm, which can be assigned to PO$_3$F$^{2−}$ and PO$_2$F$_2^-$, respectively. The relative amount of PO$_3$F$^{2−}$ in LiDFP-VC-EC/EMC is higher than that in LiDFP-EC/EMC, consistent with the ^{19}F spectrum discussed below. Since ^{19}F NMR has a relatively high sensitivity, pronounced differences can be observed between the two samples. As shown in Fig. S7, we acquired different ^{19}F spectra by applying different spin-rates to identify the real peaks and MAS induced side bands. The peaks at around −81 ppm, −135 ppm and −202 ppm can be assigned to PO$_2$F$_2^-$, PO$_3$F$^{2−}$ and LiF, respectively. Compared to the SEI layer formed in the electrolyte with only the LiDFP additive, a larger amount of PO$_3$F$^{2−}$ species is present in the surface films when cycled in LiDFP-VC-EC/EMC.

Based on these observations, the proposed mechanism behind the improvement of the long-term cyclability of the cells with the dual-additive electrolyte can be explained as follows. The VC additive promotes breaking the P–F bonds in the LiDFP additive to form more LiF, Li$_3$PO$_4$ and P–O–C species, assuming that the same amount of LiDFP participates in the formation of the SEI. Meanwhile, the passivation film formed in electrolyte containing the VC co-additive can suppress the excessive consumption of LiDFP. In combination with the formation of other organic species and suppressing the formation of Li$_2$CO$_3$, this leads to a more flexible SEI that possesses better ionic conductivity in

combination with lower electronic conductivity. This synergistic effect of VC and LiDPF raises the CE and the cycling stability of the Li-metal anode. As shown in Fig. S8, also full cells, Li/LiFePO$_4$ batteries using LiDFP-VC-EC/EMC show better cyclic stability at a fixed current density of 0.64 mA cm^{-2} with a total capacity of 0.76 mA h cm^{-2} when compared to the batteries cycled with the electrolyte without additives. Although the presented improvements are significant, especially signifying a promising rational strategy, the electrochemical performance is still far from what is necessary for application of Li-metal anodes in commercial batteries. We anticipate that, even with the dual additives, the large volumetric changes at extended cycling leads to rupture of the SEI. Future work may focus to extend the presented approach, aiming at for instance improved lithium salts to further improve the SEI.

4. Conclusions

To enable cycling of Li metal anodes in the carbonic ester electrolytes, we introduce a dual additive strategy, combining LiDFP and VC, the synergy of which results in the *in situ* formation of a mechanically stable SEI layer providing good ionic conductivity, that suppresses dendrite formation and electrolyte decomposition. After 80 cycles at a constant current density of 0.5 mA cm^{-2} with a Li deposition capacity of 1 mA h cm^{-2}, the cell maintains a CE of 95% demonstrating exceptional cycling stability compared to the cells cycled in electrolytes with individual additive. The resistance against degradation is demonstrated by stable cycling of Li/Li symmetric cells for more than 800 h at 0.5 mA cm^{-2} with a Li deposition capacity of 1 mA h cm^{-2}. The underlying mechanism is revealed by a combination of complementary electrochemical measurements and spectroscopic characterizations techniques. The co-addition of VC to the electrolyte suppresses the consumption of the LiDFP additive and facilitates the P–F bond braking during electrochemical cycling. The

resulting SEI framework of P–O–C species and other macromolecular organic compounds such as lithium ethylene dicarbonate, integrated with LiF and Li_3PO_4 inorganic species, is the origin of the improved mechanical stability and ionic conductivity of the SEI layer during prolonged cycling. This can be expected to result in a relatively homogeneous Li^+ flux, which rationalizes the dense and reversible Li deposition as directly observed through *operando* NDP. Thereby, the use of synergistic additives is demonstrated to be a promising strategy for controlling the Li-metal morphology through the *in situ* formation of a stable SEI layer. This approach can be considered to be a next step towards realizing rechargeable Li metal anodes in liquid carbonic ester electrolytes, which would be compatible with most of the existing Li battery systems in the pursue of high energy densities.

Author contributions

G. Zheng, Y. Xiang and S. Chen prepared all the samples for testing, did the electrochemical measurements, the SEM observation and the spectroscopic studies (XPS and FTIR), and analysed the data. G. Zheng, Y. Xiang, S. Ganapathy and G. Zhong measured and analysed the SSNMR data. G. Zheng and T.W. Verhallen did *operando* NDP measurements and analysed the data. M. Liu, J. Zhu, X. Han and W. Zhao contributed to the discussion of results. G. Zheng and W. Wang did the AFM detection. M. Wagemaker and Y. Yang supervised the project. G. Zheng, M. Wagemaker and Y. Yang designed the research and wrote the manuscript.

Declaration of competing interest

The authors declare no competing financial interest.

Acknowledgements

Appendix A. Supplementary data

Supplementary data to this article can be found online at https://doi.org/10.1016/j.ensm.2019.12.027.

References

[1] Y. Kim, D. Koo, S. Ha, S.C. Jung, T. Yim, H. Kim, S.K. Oh, D.M. Kim, A. Choi, Y. Kang, K.H. Ryu, M. Jang, Y.K. Han, S.M. Oh, K.T. Lee, ACS Nano 12 (2018) 4419.

[2] G. Li, Q. Huang, X. He, Y. Gao, D. Wang, S.H. Kim, D. Wang, ACS Nano 12 (2018) 1500.

[3] W. Xu, J. Wang, F. Ding, X. Chen, E. Nasybulin, Y. Zhang, J.G. Zhang, Energy Environ. Sci. 7 (2014) 513.

[4] D. Lin, Y. Liu, Y. Cui, Nat. Nanotechnol. 12 (2017) 194.

[5] H. Wu, Y. Cao, L. Geng, C. Wang, Chem. Mater. 29 (2017) 3572.

[6] Y. Liu, D. Lin, P.Y. Yuen, K. Liu, J. Xie, R.H. Dauskardt, Y. Cui, Adv. Mater. 29 (2017), 1605531.

[7] X. Shen, Y. Li, T. Qian, J. Liu, J. Zhou, C. Yan, J.B. Goodenough, Nat. Commun. 10 (2019) 900.

[8] F. Ding, W. Xu, G.L. Graff, J. Zhang, M.L. Sushko, X. Chen, Y. Shao, M.H. Engelhard, Z. Nie, J. Xiao, X. Liu, P.V. Sushko, J. Liu, J.G. Zhang, J. Am. Chem. Soc. 135 (2013) 4450.

[9] H. Zhang, G.G. Eshetu, X. Judez, C. Li, L.M. Rodriguez-Martinez, M. Armand, Angew. Chem. Int. Ed. 57 (2018), 15002.

[10] Y. Shao, H. Wang, Z. Gong, D. Wang, B. Zheng, J. Zhu, Y. Lu, Y.S. Hu, X. Guo, H. Li, X. Huang, Y. Yang, C.W. Nan, L. Chen, ACS Energy Lett. 3 (2018) 1212.

[11] M. Liu, Z. Cheng, S. Ganapathy, C. Wang, L.A. Haverkate, M. Tulodziecki, S. Unnikrishnan, M. Wagemaker, ACS Energy Lett. 4 (2019) 2336.

[12] W. Liu, D. Lin, A. Pei, Y. Cui, J. Am. Chem. Soc. 138 (2016), 15443.

[13] R. Zhang, X.R. Chen, X. Chen, X.B. Cheng, X.Q. Zhang, C. Yan, Q. Zhang, Angew. Chem. Int. Ed. 56 (2017) 7764.

[14] S. Li, M. Jiang, Y. Xie, H. Xu, J. Jia, J. Li, Adv. Mater. 30 (2018) 1706375.

[15] D. Lu, Y. Shao, T. Lozano, W.D. Bennett, G.L. Graff, B. Polzin, J. Zhang, M.H. Engelhard, N.T. Saenz, W.A. Henderson, P. Bhattacharya, J. Liu, J. Xiao, Adv. Energy Mater. 5 (2015) 1400993.

[16] X.B. Cheng, R. Zhang, C.Z. Zhao, F. Wei, J.G. Zhang, Q. Zhang, Adv. Sci. 3 (2016), 1500213.

[17] Y. Guo, H. Li, T. Zhai, Adv. Mater. 29 (2017), 1700007.

[18] J. Zheng, P. Yan, D. Mei, M.H. Engelhard, S.S. Cartmell, B.J. Polzin, C. Wang, J.G. Zhang, W. Xu, Adv. Energy Mater. 6 (2016), 1502151.

[19] J. Zhao, L. Liao, F. Shi, T. Lei, G. Chen, A. Pei, J. Sun, K. Yan, G. Zhou, J. Xie, C. Liu, Y. Li, Z. Liang, Z. Bao, Y. Cui, J. Am. Chem. Soc. 139 (2017), 11550.

[20] L. Suo, Y.S. Hu, H. Li, M. Armand, L. Chen, Nat. Commun. 4 (2013) 1481.

[21] H. Xiang, P. Shi, P. Bhattacharya, X. Chen, D. Mei, M.E. Bowden, J. Zheng, J.G. Zhang, W. Xu, J. Power Sources 318 (2016) 170.

[22] F. Qiu, X. Li, H. Deng, D. Wang, X. Mu, P. He, H. Zhou, Adv. Energy Mater. 9 (2019), 1803372.

[23] L. Suo, W. Xue, M. Gobet, S.G. Greenbaum, C. Wang, Y. Chen, W. Yang, Y. Li, J. Li, Proc. Natl. Acad. Sci. 115 (2018) 1156.

[24] M. Wang, L. Huai, G. Hu, S. Yang, F. Ren, S. Wang, Z. Zhang, Z. Chen, Z. Peng, C. Shen, D. Wang, J. Phys. Chem. C 122 (2018) 9825.

[25] S. Chen, J. Zheng, D. Mei, K.S. Han, M.H. Engelhard, W. Zhao, W. Xu, J. Liu, J.G. Zhang, Adv. Mater. 30 (2018) 1706102.

[26] J. Qian, W.A. Henderson, W. Xu, P. Bhattacharya, M. Engelhard, O. Borodin, J.G. Zhang, Nat. Commun. 6 (2015) 6362.

[27] G. Yang, Y. Li, S. Liu, S. Zhang, Z. Wang, L. Chen, Energy Storage Mater. 23 (2019) 350.

[28] J. Zheng, M.H. Engelhard, D. Mei, S. Jiao, B.J. Polzin, J.G. Zhang, W. Xu, Nat. Energy 2 (2017), 17012.

[29] T.T. Hagos, B. Thirumalraj, C.J. Huang, L.H. Abrha, T.M. Hagos, G.B. Berhe, H.K. Bezabh, J. Cherng, S.F. Chiu, W.N. Su, B.J. Hwang, ACS Appl. Mater. Interfaces 11 (2019) 9955.

[30] C. Yan, X.B. Cheng, Y. Tian, X. Chen, X.Q. Zhang, W.J. Li, J.Q. Huang, Q. Zhang, Adv. Mater. 30 (2018) 1707629.

[31] X.Q. Zhang, X. Chen, X.B. Cheng, B.Q. Li, X. Shen, C. Yan, J.Q. Huang, Q. Zhang, Angew. Chem. Int. Ed. 57 (2018) 5301.

[32] E. Markevich, G. Salitra, F. Chesneau, M. Schmidt, D. Aurbach, ACS Energy Lett. 2 (2017) 1321.

[33] K.E. Kim, J.Y. Jang, I. Park, M.H. Woo, M.H. Jeong, W.C. Shin, M. Ue, N.S. Choi, Electrochem. Commun. 61 (2015) 121.

[34] W. Zhao, G. Zheng, M. Lin, W. Zhao, D. Li, X. Guan, Y. Ji, G.F. Ortiz, Y. Yang, J. Power Sources 380 (2018) 149.

[35] P. Shi, L. Zhang, H. Xiang, X. Liang, Y. Sun, W. Xu, ACS Appl. Mater. Interfaces 10 (2018), 22201.

[36] H. Ota, K. Shima, M. Ue, J. Yamaki, Electrochim. Acta 49 (2004) 565.

[37] S. Grugeon, P. Jankowski, D. Cailleu, C. Forestier, L. Sannier, M. Armand, P. Johansson, S. Laruelle, J. Power Sources 427 (2019) 77.

[38] T.W. Verhallen, S. Lv, M. Wagemaker, Front. Energy Res. 6 (2018) 62.

[39] C. Wang, Y. Gong, J. Dai, L. Zhang, H. Xie, G. Pastel, B. Liu, E. Wachsman, H. Wang, L. Hu, J. Am. Chem. Soc. 139 (2017), 14257.

[40] S. Lv, T. Verhallen, A. Vasileiadis, F. Ooms, Y. Xu, Z. Li, Z. Li, M. Wagemaker, Nat. Commun. 9 (2018) 2152.

[41] F. Han, A.S. Westover, J. Yue, X. Fan, F. Wang, M. Chi, D.N. Leonard, N.J. Dudney, H. Wang, C. Wang, Nat. Energy 4 (2019) 187.

[42] J.F. Ziegler, M.D. Ziegler, J.P. Biersack, Nucl. Instrum. Methods Phys. Res. B 268 (2010) 1818.

[43] J.T. Maki, R.F. Fleming, D.H. Vincent, Nucl. Instrum. Methods Phys. Res. B 17 (1986) 147.

[44] R.G. Downing, J.T. Maki, R.F. Fleming, J. Radioanal. Nucl. Chem. 112 (1987) 33.

[45] B.D. Adams, J. Zheng, X. Ren, W. Xu, J.G. Zhang, Adv. Energy Mater. 8 (2018), 1702097.

[46] J. Zhang, R. Wang, X. Yang, W. Lu, X. Wu, X. Wang, H. Li, L. Chen, Nano Lett. 12 (2012) 2153.

[47] W. Xu, S.S.S. Vegunta, J.C. Flake, J. Power Sources 196 (2011) 8583.

[48] C. Wan, S. Xu, M.Y. Hu, R. Cao, J. Qian, Z. Qin, J. Liu, K.T. Mueller, J.G. Zhang, J.Z. Hu, ACS Appl. Mater. Interfaces 9 (2017), 14741.

[49] Q. Li, X. Liu, X. Han, Y. Xiang, G. Zhong, J. Wang, B. Zheng, J. Zhou, Y. Yang, ACS Appl. Mater. Interfaces 11 (2019), 14066.